Advances in Applied Mathematics and Mechanics
Adv. Appl. Math. Mech., Vol. **xx**, No. x, pp. 1-28

DOI: 10.4208/aamm.OA-2022-0183
xxx 2024

Prediction of Transition Locations in Regions of the Minor Axis of Hypersonic Elliptic Cones using the BiGlobal-e^N Method

Lei Zhao[1,2], Wenqiang Zhou[1,2], Xinliang Li[3,4], Shaolong Zhang[5] and Yongming Zhang[1,2,6,*]

[1] *Laboratory for High-Speed Aerodynamics, Tianjin University, Tianjin 300072, China*
[2] *Department of Mechanics, Tianjin University, Tianjin 300072, China*
[3] *Institute of Mechanics, Chinese Academy of Sciences, Beijing 100190, China*
[4] *School of Engineering Science, Chinese Academy of Sciences, Beijing 100049, China*
[5] *Institute of Fluid Physics, China Academy of Engineering Physics, Mianyang, Sichuan 621900, China*
[6] *Tianjin Key Laboratory of Modern Engineering Mechanics, Tianjin 300072, China*

Received 8 July 2022; Accepted (in revised version) 17 August 2023

Abstract. Two-dimensional global (BiGlobal) stability in the region of the minor axis is investigated in the case of hypersonic elliptic cones with major-minor axis ratios of 2 : 1 and 3 : 1 at Mach number 6.0, and the BiGlobal-e^N method is proposed to predict the transition location of the boundary layer. Matrix-free BiGlobal stability analysis is used to find unstable modes, including the Y-mode and the Z-mode. The growth rates in the streamwise-frequency plane for these modes are obtained. The $N_{\max\_all}$ factor is proposed, which represents the maximum amplification factor that all BiGlobal unstable modes can reach. Using a comparison of the $N_{\max\_all}$ factor with the transition location measured in a wind tunnel experiment for the 2 : 1 elliptic cone, the transition prediction criterion is determined, i.e., $N_{tr} = 8.6$. In the transition position, the amplification factors of several modes reach a level close to 8.6, which implies that none of them has the absolute superiority sufficient to cause the transition itself. Finally, the BiGlobal-e^N method is employed to predict the transition location in the region of the minor axis of the 3 : 1 elliptical cone. It is found that a larger major-minor axis ratio leads to stronger instability and an earlier transition.

AMS subject classifications: 76E99, 76K05, 76F06

Key words: BiGlobal stability, transition, boundary layer, hypersonic elliptic cone, minor axis.

*Corresponding author.
Email: ymzh@tju.edu.cn (Y. Zhang)

1 Introduction

The prediction of the transition of a boundary layer in the region of the minor axis of a hypersonic elliptical cone is closely related to practical engineering problems, and it is of great significance for scientific developments. On the one hand, to develop a next-generation hypersonic vehicle, a transition prediction in the region of the minor axis of an elliptical cone is a key problem to be solved. On the other hand, transition prediction in the region of the minor axis depends on global stability analysis, at the leading edge of the study of fluid mechanics.

The stability of the boundary layer in the region of the minor axis of a hypersonic elliptic cone is quite complicated. Even at a zero angle of attack, the streamlines on both sides of the minor axis draw close to the axis to form streamwise vortices [1], as shown in Fig. 1. As Li et al. [1] pointed out, the boundary layer here changes significantly along both the wall-normal and circumferential directions, such that the conventional stability analysis that only takes wall-normal variation into consideration is not meaningful. It is necessary to use the global stability analysis, which takes both wall-normal and circumferential variation into consideration [2–4]. Consequently, if the e^N method predicts the transitions herein, the N factors should also be obtained through global stability analysis.

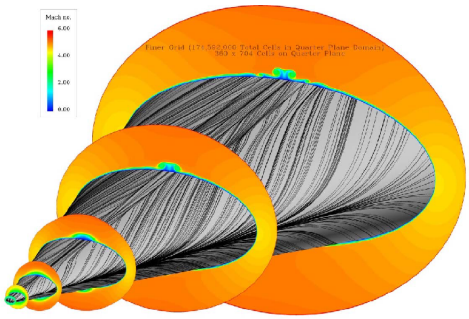

Figure 1: (color online) Basic flow of hypersonic elliptic cone HIFiRE-5 [1].

It took a historical process to understand the instability of the boundary layer and the transition in the region of the minor axis of the hypersonic elliptical cone. Basically, the historical process includes three stages. In the first stage, the streamwise vortices were not noticed. In the second stage, although the vortices were noticed, the global instability analysis method was not developed. In the last stage, the global stability instability analysis method was developed and adopted. The detailed introduction of the three stages is provided as below.

In earlier times, the streamwise vortices in the region of the minor axis were not noticed. Conventional linear stability theory (LST), which only considered wall-normal variation in the basic flow, was employed to study stability and predict transitions in the boundary layers of the elliptic cones, and the influence of crossflow was also considered.

Although studies along these lines provided some reliable results in certain regions apart from the minor axis, they could not easily explain instability in the region of the minor axis without the attention of the drastic circumferential variation in the boundary layers. Some scholars have attempted to explain the instability in the region of the minor axis in terms of second mode instability, but the results were not convincing. Lyttle and Reed [5] studied boundary layer stability for the elliptic cones with ratios of the major to the minor axis of 2:1, 3:1, and 4:1 at Mach number 4 and considered the influence of crossflow. They found that the wall-normal inflection points of the velocity profiles occurred near to the minor axis, which implies that the boundary layers were unstable here. Kimmel et al. [6] investigated stability in three cases with major-minor axis ratios of 1.5:1, 2:1, and 4:1 at Mach number 7.93 and found crossflow instabilities in all three cases. Poggie et al. [7] undertook an experiment to obtain the frequencies of the unstable disturbances close to the minor axis, with results that were consistent with those of Kimmel et al. [6]. Both Poggie et al. [7] and Kimmel et al. [6] found that the frequencies of the unstable disturbances near the minor axis were closer to those of the second mode disturbances, but no stronger evidence was provided.

Later, others began to recognize the important influence of streamwise vortices in the region of the minor axis on the boundary layer instability. However, due to a lack of an appropriate method of analysis for global stability, the traditional LST and the conventional e^N methods were used to study the stability and transition in the region of the minor axis. Schmisseur et al. [8] found the streamwise vortices in the region of the minor axis in the experiment for the 4:1 elliptical cone at Mach number 4 and supposed that the growth in disturbance was related to the vortices. Poggie et al. [7] also noticed the streamwise vortices in the experiment for the 4:1 elliptical cone at Mach number 8 and observed the earlier transition in the region of the minor axis than that in the major axis region. Huntley and Smits [9] photographed the streamwise vortices in the region of the minor axis in an experiment that involved a 4:1 elliptical cone at Mach number 8 and showed that the crossflow instability should not play the key role here. Gosse and Kimmel [10] identified the streamwise vortices in the region of the minor axis of the 2:1 elliptic cone at Mach number 7.95 and suggested that the stability analysis there should take the circumferential variation in the basic flow into consideration. Some studies focused on the HIFiRE-5 elliptical cone with major-minor axis ratio of 2:1 [11–15], with detailed parameters provided by Gosse and Kimmel [16]. Wheaton et al. [17] and Juliano et al. [18] undertook experiments on the HIFiRE-5 model at Mach number 6 in the quiet wind tunnel at Purdue University, and observed streamwise vortices along the region of the minor axis. They found that the frequencies of the unstable disturbance at the streamwise vortices were consistent with those of second mode waves but did not provide compelling evidence that the unstable disturbances were Tollmien–Schlichting (T-S) waves. Li et al. [1] conducted numerical simulations to obtain the basic flow of the HIFiRE-5 model under experimental conditions in the wind tunnel and noticed streamwise vortices in the region of the minor axis in the numerical results. Li et al. [1] claimed that conventional stability analysis that only took into account the wall-normal profiles of

the basic flow was not meaningful for addressing stability problems in the region of the minor axis due to the strong circumferential variation in the basic flow. The e^N method, which is based on traditional linear stability analysis is also unsuitable to predict transitions here. Instead, it is necessary to apply global stability analysis [19–21] and the e^N method based on global stability analysis.

In the following years, scholars began to undertake BiGlobal stability analysis in the region of the minor axis and found unstable modes. Choudhari et al. [22] carried out numerical simulations to obtain the basic flow in experimental conditions in the quiet wind tunnel of Purdue University [17, 18] and obtained a set of the BiGlobal stability analysis results in the region of the minor axis. Choudhari et al. [22] interpreted this as a new kind of unstable mode rather than a second mode perturbation. The approach of Paredes and Theofilis [23] was a milestone on the route to solving this problem. They undertook a BiGlobal stability analysis at a streamwise location of the $2:1$ elliptic cone at Mach number 7 and found four unstable modes in the region of the minor axis, including two sinuous modes and two varicose modes. Furthermore, they provided the specific method for the BiGlobal stability analysis. Paredes and Theofilis [24, 25] went on to perform a BiGlobal stability analysis at multiple streamwise locations, although they only showed the results of the most unstable sinuous mode and the most unstable varicose mode at each position. It was also found that the growth rates of the unstable modes were higher than those of the second mode waves, indicating that the unstable BiGlobal modes are different from T-S waves. Zhang [26] undertook BiGlobal stability analysis in the region of the minor axis of the HIFiRE-5 model and found two types of unstable modes. The Y-mode is related to the wall-normal shear of the basic flow, while the Z-mode corresponds to the spanwise shear. To explain the mechanism of generating these unstable modes, Li et al. [27] showed the Fjortoft inflection point area of the basic flow in the wall-normal-circumferential plane and found the eigenfunctions of the unstable modes just concentrated on the Fjortoft inflection point area, indicating that unstable modes are caused by inviscid Fjortoft inflection point instability. Moyes and Reed [28] studied the stability in the region of the minor axis of HIFiRE-5 model using a method involving parabolized stability equations based on BiGlobal stability, and compared the BiGlobal stability results with the direct numerical simulation (DNS) results and with the experimental results to verify the reliability of their method. The verified method of BiGlobal stability analysis was also applied to other problems, such as the crossflow instability [29–31].

It should be noted that the matrix method was used in the above BiGlobal stability analyses for the hypersonic boundary layers. In this method, an entire large sparse matrix is obtained, and its eigenvalue problem is solved. Although only a short period of time is necessary to calculate one case, significant memory is needed to save the matrix elements, meaning that it must be calculated with one specific computer when the mesh of the basic flow is fine enough. Zhang and Luo [32] used matrix-free BiGlobal stability analysis to investigate incompressible boundary layers. Although the matrix-free method requires a relatively long period to calculate one case, it does not employ large memory

resources, so it can run across shared computers. This matrix-free method provides more flexibility for the calculation of the BiGlobal stability analysis. Using this method, Zhang and Luo [32] obtained two kinds of unstable modes, i.e., the inner mode and the outer mode. The inner mode has relatively low phase velocity, and its eigenfunction concentrates at the bottom of the high-speed region. The outer mode has relatively high phase velocity, and its eigenfunction concentrates at the two "shoulders" of the low-speed region. In this paper, the matrix-free method is extended to the BiGlobal stability analysis of the compressible boundary layers, and BiGlobal stability in the regions of the minor axis of the hypersonic elliptic cones is investigated by using this method. Furthermore, the transition position in the region of the minor axis is predicted by the BiGlobal-e^N method based on BiGlobal stability analysis.

In this paper, elliptic cones with major-minor axis ratios of $2:1$ and $3:1$ are taken as the models to study, and a Mach number of 6 is considered for oncoming flows. DNS is used to obtain the basic flow fields. BiGlobal stability analyses are carried out for the basic flows with streamwise vortices in the regions of the minor axis, such that the growth rates of the unstable modes are obtained. The N factors are calculated by integrating the growth rates, and the $N_{\max\_all}$ factor is obtained, which represents the maximum amplification factor of all unstable modes. The $N_{\max\_all}$ factor at the transition position measured in the $2:1$ elliptical cone experiment is taken as the criterion for transition prediction, i.e., the Ntr value. Finally, the BiGlobal-e^N method is used to predict the transition in the region of the minor axis of the $3:1$ elliptic cone. In Section II, the governing equations and numerical methods of the matrix-free BiGlobal stability analysis are introduced, and the reliability of the method is verified. In Section III, the results of BiGlobal stability analyses in the regions of the minor axis of the elliptical cones and those of transition prediction by the BiGlobal-e^N method are presented.

2 Governing equations and numerical methods for BiGlobal stability analysis

2.1 Governing equations

The governing equations of the matrix-free BiGlobal stability analysis can be derived in three steps.

(i) For the dimensionless compressible Navier–Stokes (N-S) equations in the Cartesian coordinate system, instantaneous quantities are expressed as the sum of steady basic flow and disturbance quantities. By subtracting the equations corresponding to the steady basic flow from the equations for instantaneous quantities and neglecting small quantities of high orders, we obtain the linear disturbance equations.

(ii) Using the features of basic flow in the region of the minor axis of the elliptic cone, the linear disturbance equations are transformed into a curvilinear coordinate system.

(iii) Due to the characteristics of the streamwise slow variation in the basic flow, the disturbances are written in the form of streamwise waves, and frequency-free BiGlobal stability equations are obtained, which are the governing equations for matrix-free BiGlobal stability analysis. The specific derivation process is given below.

2.1.1 Linear disturbance equations in a Cartesian coordinate system

Based on the dimensional compressible N-S equations in the Cartesian coordinate system, the equations are nondimensionalized by according to the appropriate reference scales. The reference scales taken in this paper includes length scale l^* (the head radius of the elliptic cone along the direction of the minor axis, 0.95mm), oncoming free-stream velocity u_e^*, free-stream density ρ_e^*, free-stream temperature T_e^*, dynamic viscosity μ_e^*, and coefficient of thermal conductivity κ_e^*. Subscript e represents the physical quantities in the free-stream. Superscript $*$ represents dimensional quantities, and the quantities without it are dimensionless. The dimensionless N-S equations are of the form

$$\frac{\partial \rho}{\partial t}+\frac{\partial(\rho u)}{\partial x}+\frac{\partial(\rho v)}{\partial y}+\frac{\partial(\rho w)}{\partial z}=0, \tag{2.1a}$$

$$\begin{aligned}&\rho\left(\frac{\partial u}{\partial t}+u\frac{\partial u}{\partial x}+v\frac{\partial u}{\partial y}+w\frac{\partial u}{\partial z}\right)\\&=-\frac{1}{\gamma Ma^2}\frac{\partial}{\partial x}(\rho T)+\frac{1}{Re}\left\{\frac{\partial}{\partial x}\left[\mu\left(\frac{4}{3}\frac{\partial u}{\partial x}-\frac{2}{3}\frac{\partial v}{\partial y}-\frac{2}{3}\frac{\partial w}{\partial z}\right)\right]\right.\\&\quad\left.+\frac{\partial}{\partial y}\left[\mu\left(\frac{\partial u}{\partial y}+\frac{\partial v}{\partial x}\right)\right]+\frac{\partial}{\partial z}\left[\mu\left(\frac{\partial w}{\partial x}+\frac{\partial u}{\partial z}\right)\right]\right\},\end{aligned} \tag{2.1b}$$

$$\begin{aligned}&\rho\left(\frac{\partial v}{\partial t}+u\frac{\partial v}{\partial x}+v\frac{\partial v}{\partial y}+w\frac{\partial v}{\partial z}\right)\\&=-\frac{1}{\gamma Ma^2}\frac{\partial}{\partial y}(\rho T)+\frac{1}{Re}\left\{\frac{\partial}{\partial x}\left[\mu\left(\frac{\partial u}{\partial y}+\frac{\partial v}{\partial x}\right)\right]\right.\\&\quad\left.+\frac{\partial}{\partial y}\left[\mu\left(-\frac{2}{3}\frac{\partial u}{\partial x}+\frac{4}{3}\frac{\partial v}{\partial y}-\frac{2}{3}\frac{\partial w}{\partial z}\right)\right]+\frac{\partial}{\partial z}\left[\mu\left(\frac{\partial v}{\partial z}+\frac{\partial w}{\partial y}\right)\right]\right\},\end{aligned} \tag{2.1c}$$

$$\begin{aligned}&\rho\left(\frac{\partial w}{\partial t}+u\frac{\partial w}{\partial x}+v\frac{\partial w}{\partial y}+w\frac{\partial w}{\partial z}\right)\\&=-\frac{1}{\gamma Ma^2}\frac{\partial}{\partial z}(\rho T)+\frac{1}{Re}\left\{\frac{\partial}{\partial x}\left[\mu\left(\frac{\partial w}{\partial x}+\frac{\partial u}{\partial z}\right)\right]\right.\\&\quad\left.+\frac{\partial}{\partial y}\left[\mu\left(\frac{\partial v}{\partial z}+\frac{\partial w}{\partial y}\right)\right]+\frac{\partial}{\partial z}\left[\mu\left(-\frac{2}{3}\frac{\partial u}{\partial x}-\frac{2}{3}\frac{\partial v}{\partial y}+\frac{4}{3}\frac{\partial w}{\partial z}\right)\right]\right\},\end{aligned} \tag{2.1d}$$

$$\begin{aligned}&\rho\left(\frac{\partial T}{\partial t}+u\frac{\partial T}{\partial x}+v\frac{\partial T}{\partial y}+w\frac{\partial T}{\partial z}\right)\\&=\frac{(\gamma-1)}{\gamma}\left[\frac{\partial(\rho T)}{\partial t}+u\frac{\partial(\rho T)}{\partial x}+v\frac{\partial(\rho T)}{\partial y}+w\frac{\partial(\rho T)}{\partial z}\right]\\&\quad+\frac{(\gamma-1)Ma^2}{Re}\left\{2\mu\left[\left(\frac{\partial u}{\partial x}\right)^2+\left(\frac{\partial v}{\partial y}\right)^2+\left(\frac{\partial w}{\partial z}\right)^2+\frac{1}{2}\left(\frac{\partial u}{\partial y}+\frac{\partial v}{\partial x}\right)^2\right.\right.\end{aligned}$$

$$+\frac{1}{2}\left(\frac{\partial v}{\partial z}+\frac{\partial w}{\partial y}\right)^2+\frac{1}{2}\left(\frac{\partial w}{\partial x}+\frac{\partial u}{\partial z}^2\right)\Bigg]-\frac{2}{3}\mu\left(\frac{\partial u}{\partial x}+\frac{\partial v}{\partial y}+\frac{\partial w}{\partial z}\right)^2\Bigg\}$$
$$+\frac{1}{RePr}\left[\frac{\partial}{\partial x}\left(\mu\frac{\partial T}{\partial x}\right)+\frac{\partial}{\partial y}\left(\mu\frac{\partial T}{\partial y}\right)+\frac{\partial}{\partial x}\left(\mu\frac{\partial T}{\partial z}\right)\right], \tag{2.1e}$$

where x, y, and z represent the streamwise, wall-normal, and spanwise directions in the Cartesian coordinate system, respectively (see Fig. 2), and u, v, and w are the velocity components in the three corresponding directions, and t represents time. The dimensionless parameters in Eq. (2.1) include the Reynolds number $Re=\frac{\rho_e^* u_e^* l^*}{\mu_e^*}$, the Prandtl number $Pr=\frac{C_p^*\mu_e^*}{\kappa_e^*}$ (C_p^* represents the heat capacity under constant pressure), the Mach number $Ma=\frac{u_e^*}{a_e^*}$ ($a_e^*=\sqrt{\gamma R^* T_e^*}$ is the acoustic velocity in the free stream), and the specific heat ratio $\gamma=\frac{C_p^*}{C_v^*}$ (C_v^* represents the heat capacity at constant volume). The gas state equation has been used, i.e., $p=\frac{1}{\gamma Ma^2}\rho T$, where p is pressure. The Stokes assumption is applied to set the second viscosity coefficient λ^*, i.e., $\lambda^*=-\frac{2}{3}\mu^*$. The Sutherland law is employed to calculate the dynamic viscosity μ and the coefficient of thermal conductivity κ, which is of the form

$$\mu=\frac{\mu^*}{\mu_e^*}=\left(\frac{T^*}{T_e^*}\right)^{\frac{3}{2}}\frac{T_e^*+C_1^*}{T^*+C_1^*}, \tag{2.2a}$$

$$\kappa=\frac{\kappa^*}{\kappa_e^*}=\left(\frac{T^*}{T_e^*}\right)^{\frac{3}{2}}\frac{T_e^*+C_2^*}{T^*+C_2^*}, \tag{2.2b}$$

where C_1^* and C_2^* are constants, i.e., $C_1^*=C_2^*=110.4K$.

To derive the linear disturbance equation in the Cartesian coordinate system, we can express the instantaneous quantities in Eq. (2.1) as the sum of laminar basic flow and disturbance quantities, namely

$$u=\bar{u}+u'_{xyz},\quad v=\bar{v}+v'_{xyz},\quad w=\bar{w}+w'_{xyz},\quad \rho=\bar{\rho}+\rho',\quad T=\bar{T}+T',\quad \mu=\bar{\mu}+\mu', \tag{2.3}$$

where superscript $\bar{}$ represents basic flow, superscript $'$ represents the disturbance quantities, and subscript xyz indicates the disturbance velocity components in the xyz coordinate system. By substituting Eq. (2.3) into Eq. (2.1) and subtracting equation of the steady basic flow, which corresponds to the steady basic flow, one can obtain the disturbance equations. Furthermore, by neglecting higher-order terms in the disturbance equations, we can obtain linear disturbance equations in the Cartesian coordinate system, which can be expressed in the form

$$\mathrm{V}_{xx}\frac{\partial^2\phi_{xyz}}{\partial x^2}+\mathrm{V}_{yy}\frac{\partial^2\phi_{xyz}}{\partial y^2}+\mathrm{V}_{zz}\frac{\partial^2\phi_{xyz}}{\partial z^2}+\mathrm{V}_{xy}\frac{\partial^2\phi_{xyz}}{\partial x\partial y}+\mathrm{V}_{xz}\frac{\partial^2\phi_{xyz}}{\partial x\partial z}+\mathrm{V}_{yz}\frac{\partial^2\phi_{xyz}}{\partial y\partial z}$$
$$+\left(\Gamma_{xyz}\frac{\partial\phi_{xyz}}{\partial t}+\mathrm{A}_{xyz}\frac{\partial\phi_{xyz}}{\partial x}+\mathrm{B}_{xyz}\frac{\partial\phi_{xyz}}{\partial y}+\mathrm{C}_{xyz}\frac{\partial\phi_{xyz}}{\partial z}+\mathrm{D}_{xyz}\phi_{xyz}\right)=0, \tag{2.4}$$

where $\phi_{xyz}=(\rho',u'_{xyz},v'_{xyz},w'_{xyz},T')^T$ denotes the disturbance vector, and Γ_{xyz}, A_{xyz}, B_{xyz}, C_{xyz}, D_{xyz}, V_{xx}, V_{yy}, V_{zz}, V_{xy}, V_{xz} and V_{yz} are the coefficient matrices. The matrices are given in Appendix A.

2.1.2 Linear disturbance equations in curvilinear coordinates

Due to the features of basic flow in the region of the minor axis of the hypersonic elliptical cone, a curvilinear coordinate system is used. The linear disturbance equations can be acquired in two steps in a curvilinear coordinate system, enabling BiGlobal stability analysis in the region of the minor axis. The first step is to create an appropriate Cartesian coordinate system and obtain the linear disturbance equations in this coordinate system. The second step is to develop an appropriate curvilinear coordinate system and obtain the linear disturbance equations in this system via coordinate transformation.

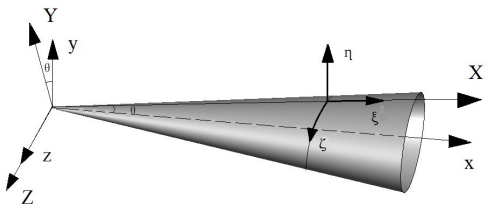

Figure 2: Schematic sketch of the coordinate systems.

The oncoming flow direction is x, and the corresponding Cartesian coordinate system xyz is shown in Fig. 2. However, in the boundary layer of the region of the minor axis, the basic flow is nearly parallel to the meridian X for the minor axis (see Fig. 2), and the disturbances also propagate downstream along the meridian. Therefore, meridian X at the minor axis is taken as the streamwise direction, and wall-normal direction Y is perpendicular to the wall at the minor axis, such that a new Cartesian coordinate system XYZ is obtained, as shown in Fig. 2. The XYZ coordinate system can be obtained by rotating the xyz coordinate system. The transformation between the xyz and XYZ coordinate systems has the form

$$\begin{cases} X=x\cos(\theta)+y\sin(\theta), \\ Y=y\cos(\theta)-x\sin(\theta), \\ Z=z, \end{cases}$$

where θ is the half-cone angle along the minor axis. The basic flow in the XYZ coordinate system can be obtained by the following equations

$$\begin{cases} \bar{U}=\bar{u}\cos(\theta)+\bar{v}\sin(\theta), \\ \bar{V}=\bar{v}\cos(\theta)-\bar{u}\sin(\theta), \\ \bar{W}=\bar{w}, \end{cases}$$

where $\bar{U}$, $\bar{V}$, and $\bar{W}$ represent the velocity components in the X, Y, and Z directions, respectively. Accordingly, the disturbance velocity components in the three directions are u', v', and w', respectively. Then the linear disturbance equations, i.e., Eq. (2.4), are transformed into the XYZ coordinate system in the following form

$$\begin{aligned}&\mathrm{V}_{XX}\frac{\partial^2\phi}{\partial X^2}+\mathrm{V}_{YY}\frac{\partial^2\phi}{\partial Y^2}+\mathrm{V}_{ZZ}\frac{\partial^2\phi}{\partial Z^2}+\mathrm{V}_{XY}\frac{\partial^2\phi}{\partial X\partial Y}+\mathrm{V}_{XZ}\frac{\partial^2\phi}{\partial X\partial Z}+\mathrm{V}_{YZ}\frac{\partial^2\phi}{\partial Y\partial Z}\\&+\left(\Gamma\frac{\partial\phi}{\partial t}+\mathrm{A}\frac{\partial\phi}{\partial X}+\mathrm{B}\frac{\partial\phi}{\partial Y}+\mathrm{C}\frac{\partial\phi}{\partial Z}+\mathrm{D}\phi\right)=0,\end{aligned}\tag{2.5}$$

where $\phi=(\rho',u',v',w',T')^T$ denotes the disturbance vector in the XYZ coordinate system, and Γ, A, B, C, D, V_{XX}, V_{YY}, V_{ZZ}, V_{XY}, V_{XZ}, and V_{YZ} are the coefficient matrices. The matrix elements are same as those in Eq. (2.4) except that they are in the new Cartesian coordinate system XYZ.

Because the surface of the elliptic cone is curves in the circumferential direction, it is necessary to use a curvilinear coordinate system $\xi\eta\zeta$, where ζ represents the circumferential direction, as shown in Fig. 2. The ξ direction coincides with the X direction, and the η direction represents the wall-normal direction, which is perpendicular to the wall. The transformation relationship between the curvilinear coordinate system $\xi\eta\zeta$ and the Cartesian coordinate system is of the form

$$\begin{cases}\xi=\xi(X),\\ \eta=\eta(Y,Z),\\ \zeta=\zeta(Y,Z).\end{cases}$$

Then we can obtain the linear disturbance equations in the $\xi\eta\zeta$ curvilinear coordinate system, namely

$$\begin{aligned}&\mathrm{V}_{\xi\xi}\frac{\partial^2\phi}{\partial\xi^2}+\mathrm{V}_{\eta\eta}\frac{\partial^2\phi}{\partial\eta^2}+\mathrm{V}_{\zeta\zeta}\frac{\partial^2\phi}{\partial\zeta^2}+\mathrm{V}_{\xi\eta}\frac{\partial^2\phi}{\partial\xi\partial\eta}+\mathrm{V}_{\xi\zeta}\frac{\partial^2\phi}{\partial\xi\partial\zeta}+\mathrm{V}_{\eta\zeta}\frac{\partial^2\phi}{\partial\eta\partial\zeta}\\&+\left(\Gamma\frac{\partial\phi}{\partial t}+\mathrm{A}_{\xi\eta\zeta}\frac{\partial\phi}{\partial\xi}+\mathrm{B}_{\xi\eta\zeta}\frac{\partial\phi}{\partial\eta}+\mathrm{C}_{\xi\eta\zeta}\frac{\partial\phi}{\partial z}+\mathrm{D}\phi\right)=0,\end{aligned}\tag{2.6}$$

where $\phi=(\rho',u',v',w',T')^T$ denotes the disturbance vector in the XYZ coordinate system, and $\mathrm{A}_{\xi\eta\zeta}$, $\mathrm{B}_{\xi\eta\zeta}$, $\mathrm{C}_{\xi\eta\zeta}$, $\mathrm{V}_{\xi\xi}$, $\mathrm{V}_{\eta\eta}$, $\mathrm{V}_{\zeta\zeta}$, $\mathrm{V}_{\xi\eta}$, $\mathrm{V}_{\xi\zeta}$, and $\mathrm{V}_{\eta\zeta}$ represent the coefficient matrices. The matrices are shown in Appendix B.

2.1.3 Frequency-free BiGlobal linear stability equations

Due to the streamwise vortices in the region of the minor axis of the elliptical cone, the variation in basic flow along the wall-normal and circumferential directions is quite strong. However, the basic flow only changes slowly along the streamwise direction.

Therefore, we can apply the hypothesis of the quasi-parallel flow, such that the disturbances can be expressed as the form of streamwise waves, namely,

$$\phi(\xi,\eta,\zeta,t)=\tilde{\phi}(\eta,\zeta,t)e^{i\alpha\xi}+c.c., \tag{2.7}$$

where α represents the streamwise wavenumber, $\tilde{\phi}=\left(\tilde{\rho},\tilde{u},\tilde{v},\tilde{w},\tilde{T}\right)^T$ represents the streamwise wave vector, and $c.c.$ represents the complex conjugate. By substituting Eq. (2.7) into the linear disturbance equations, i.e., Eq. (2.6), we obtain the equations for $\tilde{\phi}$ in the form

$$\Gamma\frac{\partial\tilde{\phi}}{\partial t}+\tilde{B}\frac{\partial\tilde{\phi}}{\partial\eta}+\tilde{C}\frac{\partial\tilde{\phi}}{\partial\zeta}+\mathrm{V}_{\eta\eta}\frac{\partial^2\tilde{\phi}}{\partial\eta^2}+\mathrm{V}_{\zeta\zeta}\frac{\partial^2\tilde{\phi}}{\partial\zeta^2}+\mathrm{V}_{\eta\zeta}\frac{\partial^2\tilde{\phi}}{\partial\eta\partial\zeta}+\tilde{D}\tilde{\phi}=0, \tag{2.8}$$

where $\tilde{B}$, $\tilde{C}$, and $\tilde{D}$ are the coefficient matrices. The matrices can be expressed as below

$$\begin{cases}\tilde{B}=B+i\alpha\mathrm{V}_{\xi\eta},\\ \tilde{C}=C+i\alpha\mathrm{V}_{\xi\zeta},\\ \tilde{D}=D+i\alpha\mathrm{A}-\alpha^2\mathrm{V}_{\xi\xi}.\end{cases}$$

Eq. (2.8) is the governing equation for the matrix-free BiGlobal linear stability analysis, i.e., frequency-free BiGlobal linear stability equations.

For Eq. (2.8), the no-slip and isothermal boundary conditions are adopted on the wall, namely

$$\tilde{u}=\tilde{v}=\tilde{w}=\tilde{T}=0 \quad \text{at } \eta=0.$$

At the top boundary of the computational domain, which is far from the wall, the perturbation amplitude tends to zero, so the boundary condition is taken as

$$\tilde{\rho}=\tilde{u}=\tilde{v}=\tilde{w}=\tilde{T}=0 \quad \text{as } \eta\to\infty.$$

2.2 Numerical methods

2.2.1 Numerical differential methods

To solve Eq. (2.8), we use the following numerical methods. In the circumferential direction, the spectral method is employed, and the Fourier series is taken as the base function family, which is of the form

$$f(\eta,\zeta,t)=\sum_{n=-\infty}^{+\infty}\breve{f}(\eta,t)e^{in\beta\zeta},$$

where f and $\breve{f}$ represent the functions in the physical and spectral space, respectively, and β is the circumferential fundamental wavenumber. In the wall-normal direction,

the fourth-order central difference schemes are used for the first and second derivatives, namely

$$\left(\frac{\partial f}{\partial \eta}\right)_j = \frac{f_{j-2}-8f_{j-1}+8f_{j+1}-f_{j+2}}{12\Delta\eta}+\mathcal{O}((\Delta\eta)^4),$$
$$\left(\frac{\partial^2 f}{\partial \eta^2}\right)_j = \frac{-f_{j-2}+16f_{j-1}-30f_j+16f_{j+1}-f_{j+2}}{12\Delta\eta^2}+\mathcal{O}((\Delta\eta)^4).$$

We can only use lower order schemes near the wall. At the point $j=N-1$, the third-order schemes were adopted, which are of the form

$$\left(\frac{\partial f}{\partial \eta}\right)_{N-1} = \frac{f_{N-3}-6f_{N-2}+3f_{N-1}+2f_N}{6\Delta\eta}+\mathcal{O}((\Delta\eta)^3)$$
$$\left(\frac{\partial^2 f}{\partial \eta^2}\right)_{N-1} = \frac{f_{N-2}-2f_{N-1}+f_N}{\Delta\eta^2}+\mathcal{O}((\Delta\eta)^3).$$

At the point $j=1$, the difference schemes are

$$\left(\frac{\partial f}{\partial \eta}\right)_1 = \frac{-2f_0-3f_1+6f_2-f_3}{6\Delta\eta}+\mathcal{O}((\Delta\eta)^3),$$
$$\left(\frac{\partial^2 f}{\partial \eta^2}\right)_1 = \frac{f_0-2f_1+f_2}{\Delta\eta^2}+\mathcal{O}((\Delta\eta)^3).$$

At the top boundary point $j=N$, the second-order schemes are used, which are of the form

$$\left(\frac{\partial f}{\partial \eta}\right)_N = \frac{f_{N-2}-4f_{N-1}+3f_N}{6\Delta\eta}+\mathcal{O}((\Delta\eta)^2),$$
$$\left(\frac{\partial^2 f}{\partial \eta^2}\right)_N = \frac{f_{N-2}-2f_{N-1}+f_N}{\Delta\eta^2}+\mathcal{O}((\Delta\eta)^2).$$

At the wall point $j=0$, the difference schemes are

$$\left(\frac{\partial f}{\partial \eta}\right)_0 = \frac{-3f_0+4f_1-f_2}{2\Delta\eta}+\mathcal{O}((\Delta\eta)^2)$$
$$\left(\frac{\partial^2 f}{\partial \eta^2}\right)_0 = \frac{f_0-2f_1+f_2}{\Delta\eta^2}+\mathcal{O}((\Delta\eta)^2).$$

The third-order difference scheme is used for time splitting, namely

$$\left(\frac{\partial f}{\partial t}\right)_i = \frac{11}{6\Delta t}f_i+\left(\frac{-3}{\Delta t}\right)f_{i-1}+\frac{3}{2\Delta t}f_{i-2}+\frac{-1}{3\Delta t}f_{i-3}+\mathcal{O}((\Delta t)^3).$$

2.2.2 Eigenvalue problem of matrix-free BiGlobal stability analysis

The frequency-free BiGlobal linear stability equations Eq. (2.8) are linear equations concerning $\tilde{\phi}$. Therefore, for a fixed wavenumber α, the linear stability equations define the linear evolution operator $L(t,\alpha)$, which can be expressed as

$$\tilde{\phi}(\eta,\zeta,t) = L(t,\alpha)\tilde{\phi}(\eta,\zeta,0). \tag{2.9}$$

Taking a fixed time interval T_0, we can obtain the linear evolution relationship as

$$\tilde{\phi}(\eta,\zeta,T_0) = L(T_0,\alpha)\tilde{\phi}(\eta,\zeta,0). \tag{2.10}$$

$L(T_0,\alpha)$ is still a linear operator, so it has eigenmodes, which can be expressed as

$$L(T_0,\alpha)\hat{\phi}(\eta,\zeta) = \hat{\lambda}\hat{\phi}(\eta,\zeta), \tag{2.11}$$

where $\hat{\lambda}$ and $\hat{\phi}(\eta,\zeta)$ represent the eigenvalue and eigenfunction for an eigenmode, respectively.

In another way, due to Eq. (2.8), for an eigenmode, the evolution of the corresponding $\tilde{\phi}$ from $t=0$ to $t=T_0$ can also be described in the form of the complex frequency

$$\tilde{\phi}(\eta,\zeta,T_0) = e^{-i\omega T_0}\tilde{\phi}(\eta,\zeta,0), \tag{2.12}$$

where $\omega = \omega_r + \omega_i$ is the complex frequency, the real part ω_r denotes the real frequency, and the imaginary part ω_i denotes the growth rate for temporal mode problem. Then the eigenmode can be described as

$$L(T_0,\alpha)\hat{\phi}(\eta,\zeta) = e^{-i\omega T_0}\hat{\phi}(\eta,\zeta). \tag{2.13}$$

From Eqs. (2.11) and (2.13), we obtain the relationship between the eigenvalue $\hat{\lambda}$ and the frequency ω as

$$\hat{\lambda} = e^{-i\omega T_0}. \tag{2.14}$$

We use ω to represent the eigenvalue for the temporal mode problem below.

We can obtain the evolution of $\tilde{\phi}$ from $t=0$ to $t=T_0$ by solving Eq. (2.8), and we can obtain the eigenvalues $\hat{\lambda}$ and eigenfunctions $\hat{\phi}(\eta,\zeta)$ of the linear operator $L(T_0,\alpha)$ using the Arnoldi iterative method. Here, the Arnoldi method is implemented by calling the open source package ARPACK. The detailed numerical methods for this step were provided by Lehoucq et al. [33] and Zhang and Luo [32], and they are not repeated here.

2.2.3 Verification of matrix-free BiGlobal stability analysis method for compressible flows

Zhao et al. [29] applied matrix BiGlobal stability analysis to study the stability of the hypersonic streaky boundary layer over a flat plate with a blunt leading edge, and the results were verified by the comparison with the DNS results. In this paper, our matrix-free

Table 1: Parameters of the hypersonic streaky boundary layer.

Ma	$T_e^*(K)$	Re (Nose radius is taken as the length scale)	Pr
5.96	87.0	3.34×10^4	0.72

Table 2: Eigenvalues of the unstable modes of the hypersonic streaky boundary layer.

Mode	Method	α	ω_r	ω_i
1	Matrix-free BiGlobal (Current method)	0.9	0.609143	0.05385
	Matrix BiGlobal (Zhao et al. [29])	0.9	0.609102	0.05386
2	Matrix-free BiGlobal (Current method)	0.9	0.624851	0.03919
	Matrix BiGlobal (Zhao et al. [29])	0.9	0.624826	0.03925
3	Matrix-free BiGlobal (Current method)	0.9	0.650545	0.01337
	Matrix BiGlobal (Zhao et al. [29])	0.9	0.650413	0.01311

BiGlobal stability method was employed for the stability analysis of the streaky boundary layer, and the results are compared to those of Zhao et al. [29] for verification. The parameters of the hypersonic streaky boundary layer are listed in Table 1.

The eigenvalues of three unstable modes obtained using the current matrix-free BiGlobal method are shown in Table 2 and are consistent with those of Zhao et al. [29] by the matrix BiGlobal method. The above verification confirms that the matrix-free BiGlobal stability analysis is reliable.

3 Results and discussion

3.1 Elliptical cone a ratio of major to minor axis of $2:1$

3.1.1 Model parameters and basic flow

In this paper, the $2:1$ elliptic cone model is a 38.1% scale model of HIFiRE-5. Juliano et al. [18] performed experimental investigation of the 38.1% model in a wind tunnel, so we can compare our results with the experimental data. The cross section of the cone is elliptic, and the ratio of major-minor axis is $2:1$. Along the direction of the minor axis, the radius of the nose is 0.95mm, and the half cone angle θ is 7°. The length of the model is 328mm, and the minor axis radius of the cross section is 41mm at the tail end of the model. More specific parameters were provided by Juliano et al. [18]. Although this vehicle model is smaller than that of Paredes and Theofilis [23–25], we can still compare our results with those of Paredes and Theofilis [23–25] qualitatively.

Table 3: Conditions for the basic flow calculation.

Ma	$Re_{\text{unit}}(m^{-1})$	$T_e^*(K)$	$T_w^*(K)$	AOA($^\circ$)
6.0	10.2×10^6	52.0	300.0	0.0

The working conditions here are the same as those for Juliano et al. [18], as shown in Table 3. In the table, $Re_{\text{unit}}=\rho_e^* u_e^*/\mu_e^*$ is the unit Reynolds number, T_w^* is the wall temperature, and AOA is the angle of attack. At a zero angle of attack, the basic flow is symmetrical, so it is sufficient to take a quarter of the model and to adopt the symmetric boundary condition in the circumferential direction. The free-stream condition is applied in the far field, and the no-slip and isothermal conditions are employed on the wall. The outlet of the computational domain is taken at $x^*=381$mm, and the linear extrapolation condition is adopted at the outlet. We take 400, 300, and 300 grid points in the streamwise, wall-normal, and circumferential directions, respectively. In the wall-normal direction, more than 100 grid points are taken in the boundary layer. Li et al. [1] conducted a comprehensive analysis of mesh convergence. According to results of Li et al. [1], our grid satisfies the convergence condition. In this paper, the basic flow is obtained by DNS, and detailed numerical methods were presented by Zhao [34] and Song et al. [35].

Fig. 3 shows the streamwise velocity distribution in the wall-normal-spanwise plane at different streamwise locations, where $\bar{U}$ represents the local streamwise velocity, and

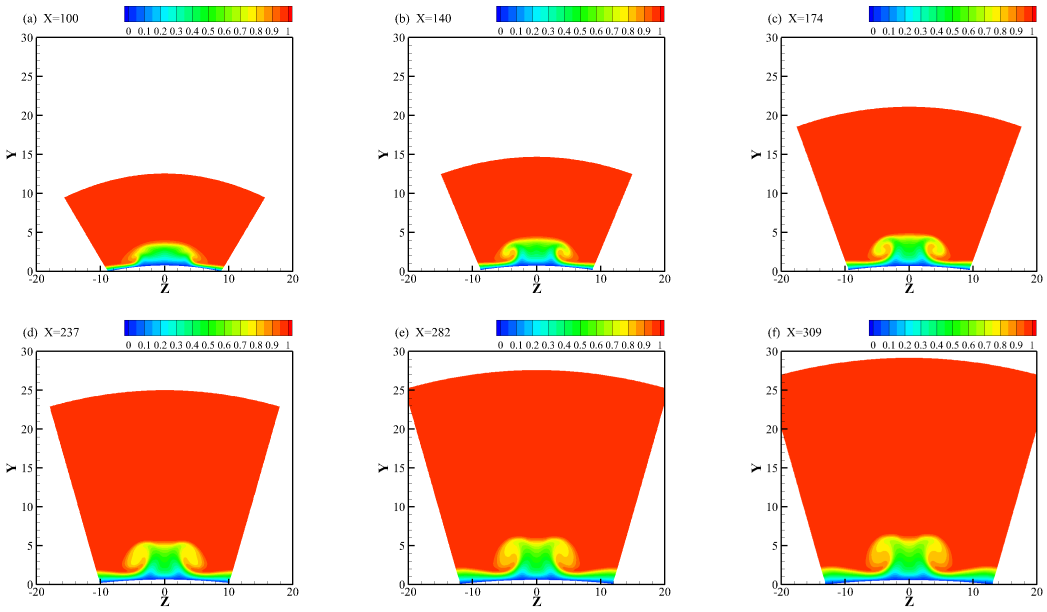

Figure 3: (color online) Contour of velocity $\bar{U}/\bar{U}_{\max}$ in the wall-normal-spanwise plane in the region of the minor axis. (a) $X=100$. (b) $X=140$. (c) $X=174$. (d) $X=237$. (e) $X=282$. (f) $X=309$.

$\bar{U}_{\max}$ representes the maximum stream velocity in the flow field. The figure indicates that the streamwise evolution of vortices is quite slow. From $X=105$, the spanwise width of the streamwise vortices continue unchanged, and the wall-normal height grows slowly. Therefore, the dependence of the basic flow on the streamwise direction X can be treated as being parametric when the BiGlobal stability in the wall-normal-spanwise plane is considered in the region of the minor axis, as noted by Zhang et al. [36].

3.1.2 Results of BiGlobal stability analysis

We perform BiGlobal stability analysis of the basic flow in the region of the minor axis at $X=191$ and find two kinds of unstable outer modes, i.e., the Y-mode and the Z-mode, and we do not find an unstable inner mode. The eigenfunctions of the Y-mode and the Z-mode and the contour of the basic flow $\bar{U}$ are shown in Fig. 4. The eigenfunction of the Y-mode is concentrated on two shoulders of the mushroom, and stretches along the spanwise direction, as shown in Fig. 4(a). This means that the Y-mode is caused by the shear of the basic flow along the wall-normal direction, giving rise to its name. Fig. 4(b) shows that the eigenfunction of the Z-mode is concentrated on the waist of the mushroom, and the eigenfunction stretches along the wall-normal direction. This implies that the Z-mode is caused by the shear of the basic flow along the spanwise direction, and this is why it is called Z-mode.

The eigenfunctions of the unstable modes and the Fjortoft inflection points of the basic flow in the Y-Z plane are shown in Fig. 5. The Fjortoft inflection points satisfy the conditions

$$\begin{cases} \dfrac{\partial}{\partial s}\left(\rho\dfrac{\partial \bar{U}_I}{\partial s}\right)=0, \\ \dfrac{\partial}{\partial s}\left(\rho\dfrac{\partial \bar{U}_I}{\partial s}\right)(\bar{U}-\bar{U}_I)<0, \end{cases} \tag{3.1}$$

where s is the gradient direction of the basic flow $\bar{U}$ in the Y-Z plane, $\partial/\partial s$ is the derivative along the gradient direction, and $\bar{U}_I$ is the basic flow at the inflection point. In Fig. 5, the

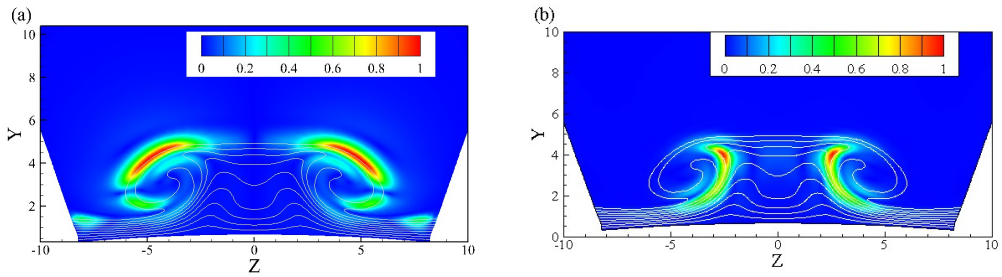

Figure 4: (color online) Contour of eigenfunctions $|\hat{u}|/|\hat{u}|_{\max}$ for the Y-mode and the Z-mode. The color contours represent eigenfunctions. The white lines are the contour lines of the basic flow $\bar{U}$. (a) Y-mode. (b) Z-mode.

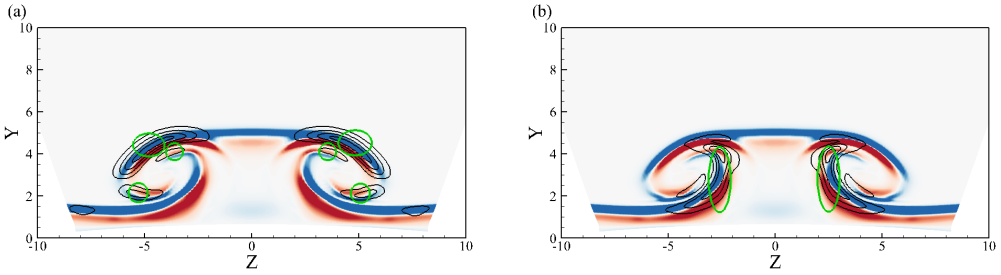

Figure 5: (color online) Eigenfunctions of the unstable modes and Fjortoft-inflection-points of the basic flow. Black lines: contour of the eigenfunction $|\hat{u}|/|\hat{u}|_{\max}$ of the unstable modes. Red contour: positive second derivative of the basic flow in the gradient direction in Y-Z plane. Blue contour: negative second derivative. White contour: second derivative is zero. Green circles: Fjortoft inflection points. (a) Y-mode. (b) Z-mode.

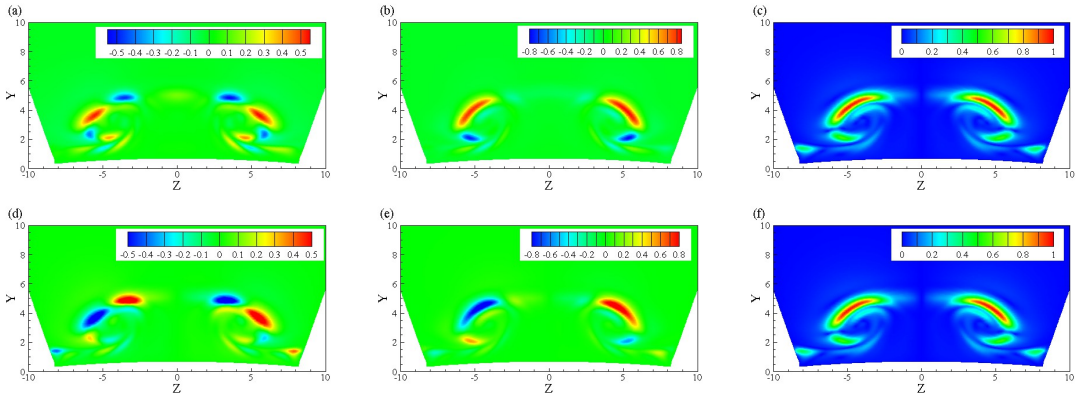

Figure 6: (color online) Eigenfunctions of the varicose type (a), (b), and (c) and sinuous type (d), (e), and (f)) Y-modes. (a) and (d): $\hat{u}_r$. (b) and (e): $\hat{u}_i$. (c) and (f): $|\hat{u}|$. The results are normalized by $|\hat{u}|_{\max}$.

black lines represent the contour of the eigenfunction modulus $|\hat{u}|/|\hat{u}|_{\max}$, and the green circles mark the Fjortoft inflection points. For both the Y-mode and the Z-mode, the eigenfunctions concentrate on the Fjortoft inflection points, indicating that the instability of the modes are caused by the inflectional instability of the shear flow.

In this paper, multiple unstable Y-modes and Z-modes are found. The Y-modes can be classified into two types, sinuous and varicose, as can the Z-modes. The eigenfunction $\hat{u}$ of the sinuous mode is anti-symmetric in the spanwise direction, while that of the varicose mode is symmetric. Fig. 5 shows the eigenfunction $\hat{u}$ of a varicose Y-mode at a streamwise position $(X=191)$, including the real part $\hat{u}_r$, imaginary part $\hat{u}_i$, and modulus $|\hat{u}|$, along with the results of a sinuous Y-mode. The eigenfunction shape of sinuous Y-mode in Fig. 5 is qualitatively consistent with that of the anti-symmetric mode obtained by Paredes and Theofilis [23–25] for a larger vehicle model. Similarly, the eigenfunction shape of varicose Y-mode in Fig. 5 is qualitatively consistent with that of the symmetric mode in references [23–25]. The modulus $|\hat{u}|$ of the varicose mode is the same as that of

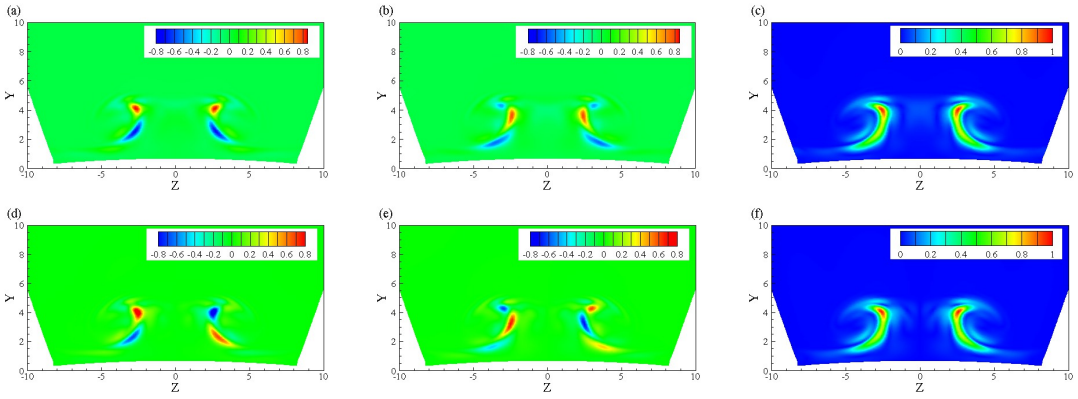

Figure 7: (color online) Eigenfunctions of the varicose type (a), (b), and (c) and sinuous type (d), (e), and (f) Z-modes. (a) and (d): $\hat{u}_r$. (b) and (e): $\hat{u}_i$. (c) and (f): $|\hat{u}|$. The results are normalized by $|\hat{u}|_{\max}$.

the sinuous mode. However, both the real part $\hat{u}_r$and the imaginary part $\hat{u}_i$ of the varicose modes are symmetrical in the spanwise direction, while those of the sinuous mode are anti-symmetrical. Similarly, the eigenfunctions of the varicose type and sinuous type Z-modes are shown in Fig. 7.

The matrix-free BiGlobal stability analysis is performed with respect to the temporal mode problem. However, for the disturbance evolution in the boundary layer, it is more appropriate to describe the growth of unstable modes via the spatial mode. It is therefore necessary to obtain the growth rate of spatial mode $-\alpha_i$. In this paper, we calculate $-\alpha_i$ using the Gaster transform [37], which is of the form

$$-\alpha_i = \omega_i / c_g, \tag{3.2}$$

where $c_g = \partial\omega_r/\partial\alpha$ is the group velocity. We apply the approximation $c_g \approx \Delta\omega_r/\Delta\alpha$ to calculate the group velocity, and $\Delta\alpha$ is taken as 0.001, which is small enough to obtain the converged numerical results. We only show the spatial mode results below.

We find several unstable modes, and we focus on six of them to discuss in this paper, namely the three most unstable Y-modes (Y-mode 1, Y-mode 2, and Y-mode 3) and the three most unstable Z-modes (Z-mode 1, Z-mode 2, and Z-mode 3). Y-mode 1 and Z-mode 1 are varicose, and the other four are sinuous. Fig. 8 shows contours of the growth rates $-\alpha_i$ of the six modes in the streamwise-frequency (X-F) plane, where F is the dimensionless frequency defined as $F = 2\pi f^* v_e^* / U_e^{*2}$, where f^* is dimensional frequency, and v_e^* is kinematic viscosity. The growth rates of Y-mode 1 and Y-mode 2 are relatively high, and that of Y-mode 3 is low. The results for the Z-modes are similar, but the unstable frequency bandwidths are narrower.

3.1.3 Results of BiGlobal-e^N method

The traditional e^N method [38, 39] is based on the traditional stability analysis. Disturbance amplification factor N is obtained by integrating the growth rate, and the envelope

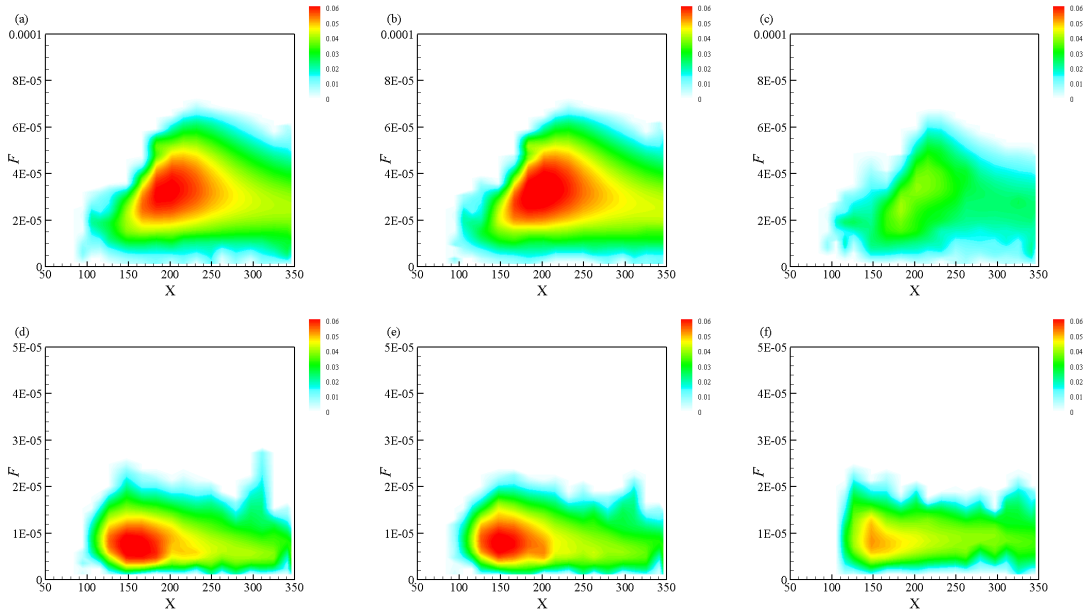

Figure 8: (color online) Contours of the growth rate $-\alpha_i$ of the unstable modes in the $X-F$ plane. (a) Y-mode 1. (b) Y-mode 2. (c) Y-mode 3. (d) Z-mode 1. (e) Z-mode 2. (f) Z-mode 3.

of the N factor, i.e., the $N_{\max}$ factor, is compared to the critical value N_{tr}, such that the transition location can be predicted. We borrow the idea of the traditional e^N method, but we calculate the N factors of unstable modes based on the results of the BiGlobal stability analysis. So this method is named as BiGlobal-e^N method.

The N factor is defined as the integral of the growth rate of an unstable mode at the frequency F, which is expressed as

$$N(F,X)=\int_{X_0}^{X}-\alpha_i dX, \tag{3.3}$$

where X_0 is the critical location where the disturbance becomes unstable. The N factor represents the logarithm of the growth multiple of the disturbance, namely

$$N=\ln\left[\frac{A(X)}{A(X_0)}\right], \tag{3.4}$$

where A is the amplitude of the disturbance.

Fig. 9 shows the N factor contours of the six unstable modes in the $X-F$ plane. The N factors grow up to the cone tail. The N factors of Y-mode 1, Y-mode 2, Z-mode 1, and Z-mode 2 are relatively high, while the results for Y-mode 3 and Z-mode 3 are low. For Y-mode 1 and Y-mode 2, the frequencies F corresponding to the maximum N factor are about 2.5×10^{-5}. For Z-mode 1 and Z-mode 2, the corresponding frequencies F are about 0.6×10^{-5}.

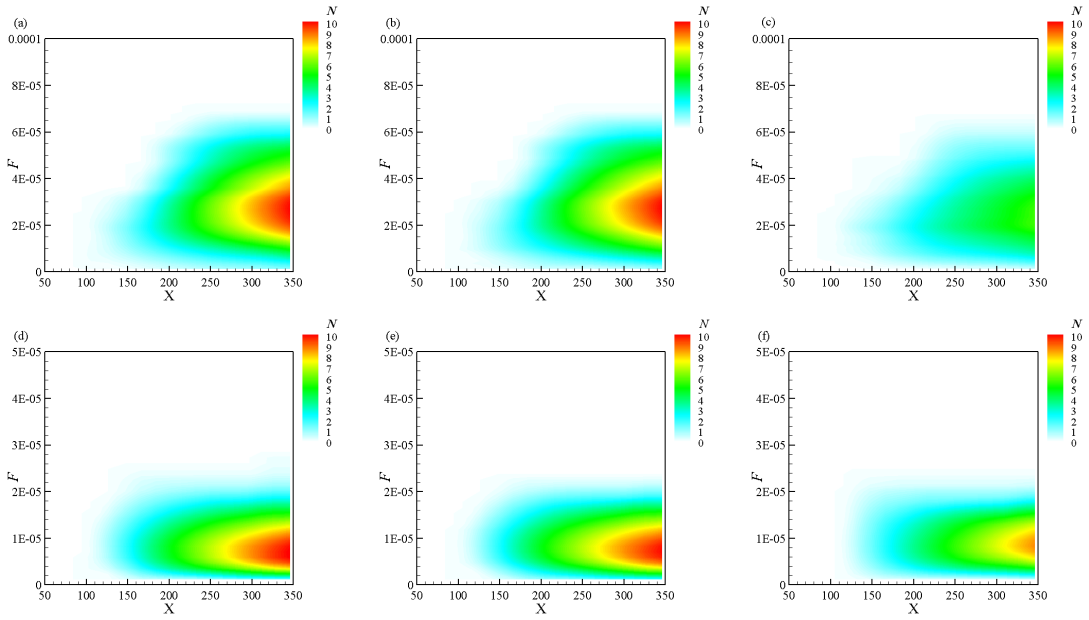

Figure 9: (color online) Contours of factor N in the $X-F$ plane. (a) Y-mode 1. (b) Y-mode 2. (c) Y-mode 3. (d) Z-mode 1. (e) Z-mode 2. (f) Z-mode 3.

Continuing to use the traditional e^N method as a reference, we plot the maximum N factor at each streamwise location, i.e., the $N_{\max}$ factor and the $N_{\max}$ factors of the six unstable modes in Fig. 10(a). For one mode, the $N_{\max}$ factor curve in the figure is also the envelope of the N factor curves at different frequencies. The $N_{\max}$ factor of each mode increases monotonically along the streamwise direction until the cone tail, and the $N_{\max}$ curves of several modes intersect. For the four most unstable modes, i.e., Y-mode 1, Y-mode 2, Z-mode 1, and Z-mode 2, the $N_{\max}$ factors reach about 10.5. The $N_{\max}$ factor of Z-mode 3 grows to about 9, and that of Y-mode 3 only reaches about 5.5.

Fig. 10(a) shows the growth of several unstable modes found via the BiGlobal stability analysis, but it is not simple to predict the transition based on the several $N_{\max}$ curves in the figure. To provide an easy method of transition prediction, we take the envelope of the $N_{\max}$ curves to obtain just one curve, i.e., the $N_{\max\_all}$ curve, as shown in Fig. 11. The $N_{\max\_all}$ curve represents the maximum amplification factor that all unstable modes can achieve under conservative estimates. To predict the transition location, we still require the transition prediction criterion, i.e., the critical value N_{tr}. According to the basic idea of the e^N method, the transition criterion should be calibrated by experiment. The wind tunnel experiment of Juliano et al. [18] was undertaken under the same conditions as our calculation above. The experimental results showed that the transition position in the minor axis region is $X_{tr}=284$, where $N_{\max\_all}$ is 8.6, as shown in Fig. 11. Therefore, $N_{tr}=8.6$ is taken as the transition criterion of the BiGlobal-e^N method. Furthermore,

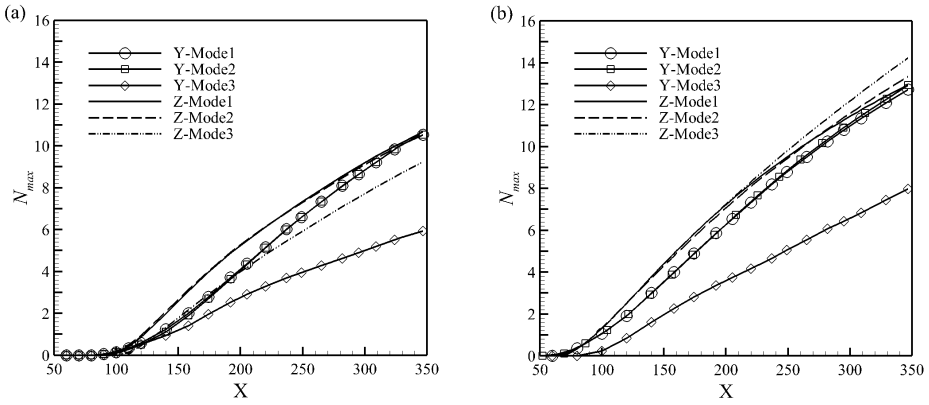

Figure 10: $N_{\max}$ factors for the 2:1 and 3:1 elliptic cones. (a) 2:1. (b) 3:1.

Fig. 10(a) shows that the $N_{\max}$ factor of Z-mode 1 is the highest at the transition location, which is 8.6. However, the $N_{\max}$ factors of the other three modes, i.e., Y-mode 1, Y-mode 2, and Z-mode 2, are also quite close to 8.6 at $X=284$. This indicates that several modes are sufficiently or almost sufficiently amplified to trigger transition at this location, and none of them has an absolute leading superiority to allow it to cause transition itself.

3.2 Elliptical cone with major-minor axis ratio of 3:1

Using the 2:1 elliptic cone model in the previous section, the length of the major axis is changed to three times that of the minor-axis, and the other parameters remain unchanged, such that we obtain the 3:1 elliptic cone model. The oncoming flow parameters are the same as those in the 2:1 elliptic cone, and basic flow is also obtained by DNS. The basic flow is similar to that of the 2:1 elliptic cone, and there are also streamwise vortices in the region of the minor axis.

The BiGlobal stability analysis shows that there are also two kinds of unstable outer modes in the region of the minor axis, i.e., the Y-mode and Z-mode, and no unstable inner mode is found. Similar to the results of the 2:1 elliptical cone, the unstable Y-modes include varicose type and sinuous type, as do the Z-modes. However, the unstable modes for the 3:1 elliptic cone are stronger than those for the 2:1 elliptic code. We still take six modes to study, including the three most unstable Y-modes and the three most unstable Z-modes. Fig. 10(b) shows the $N_{\max}$ factors of the six unstable modes along the streamwise direction. At the tail of the elliptical cone, the $N_{\max}$ factors of Y-mode 1, Y-mode 2, Z-mode 1, and Z-mode 2 reach about 13. The $N_{\max}$ factor of Z-mode 3 rises to about 14, while that of Y-mode 3 only reaches about 7.5. The $N_{\max}$ factors for the 3:1 elliptical cone are significantly higher than those for the 2:1 elliptical cone. This implies that the larger ratio of major to minor axis could promote the growth of the unstable modes in the region of the minor axis.

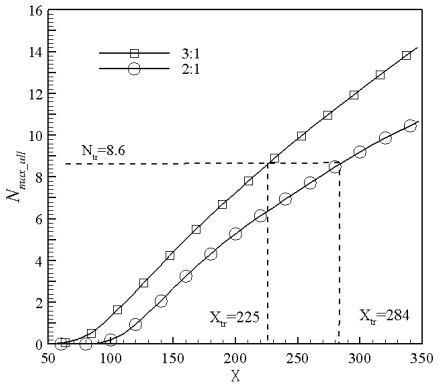

Figure 11: $N_{\max\_all}$ factors for the 2:1 and 3:1 elliptic cones.

Fig. 11 shows the envelope of the $N_{\max}$ factors of the unstable modes, i.e., the $N_{\max\_all}$ factor. The results of the 2:1 elliptical cone are also plotted in the figure. The $N_{\max\_all}$ factor of the 3:1 elliptic cone is always higher than that of the 2:1 elliptic cone, indicating that larger major to minor axis ratios lead to earlier transitions at the minor axis. According to the calibrated transition criterion $N_{tr}=8.6$, the predicted the transition position in the region of the minor axis of the 3:1 elliptic cone is $X_{tr}=225$, which is about 20% forward of the transition location of the 2:1 elliptic cone. This means that a larger ratio of major to minor axis leads to an earlier transition in the region of the minor axis of the elliptic cone.

4 Conclusions

In this paper, we employ matrix-free BiGlobal stability analysis to investigate the stability of the boundary layer with streamwise vortices in the region of the minor axis of the hypersonic elliptic cones with ratios of major to minor axis of 2:1 and 3:1. From the results of the stability analysis, we apply the BiGlobal-e^N method to predict the transition position, and we draw the following conclusions.

(1) There are two kinds of unstable outer modes in the boundary layer in the region of the minor axis of the hypersonic elliptic cones, namely the Y-mode and the Z-mode, and no unstable inner mode is found.

(2) The eigenfunctions of the unstable modes concentrate on the Fjortoft inflection point areas in the wall-normal-spanwise plane, indicating that the BiGlobal unstable modes in the region of the minor axis are caused by the inflectional instability of the basic flow.

(3) For one unstable mode, the $N_{\max}$ factor can be obtained by taking the envelope of the N factor curves at different frequencies, indicating the maximum amplification

factor that the mode can achieve. The $N_{\max\_all}$ factor can be obtained by taking the envelope of the $N_{\max}$ factor curves of different modes, indicating the maximum amplification factor that all of the unstable modes can achieve. The position where the $N_{\max\_all}$ factor curve reaches the critical value N_{tr} is considered the transition position. Using the location of the transition of the 2:1 elliptic cone measured in the wind tunnel experiment of Juliano et al. [18], the critical value is taken as $N_{tr}=8.6$. At the transition location, the $N_{\max}$ factors of several modes are close to the critical level of 8.6, indicating that none of them plays the dominant role in causing the transition.

(4) The BiGlobal-e^N method is employed to predict the transition location in the region of the minor axis of the 3 : 1 elliptic cone. A comparison of the results of the 3 : 1 elliptic cone with those of the 2:1 elliptical cone indicates that a larger major-minor axis ratio causes stronger instability and an earlier transition.

Appendix A: The coefficient matrices in Eq. (2.4)

The coefficient matrices in Eq. (2.4) are shown as below

$$\mathbf{V}_{xx}=\begin{pmatrix}0&0&0&0&0\\0&-\frac{4}{3}\frac{1}{Re}\bar{\mu}&0&0&0\\0&0&-\frac{1}{Re}\bar{\mu}&0&0\\0&0&0&-\frac{1}{Re}\bar{\mu}&0\\0&0&0&0&-\frac{1}{RePr}\bar{\mu}\end{pmatrix},\quad \mathbf{V}_{yy}=\begin{pmatrix}0&0&0&0&0\\0&-\frac{1}{Re}\bar{\mu}&0&0&0\\0&0&-\frac{4}{3}\frac{1}{Re}\bar{\mu}&0&0\\0&0&0&-\frac{1}{Re}\bar{\mu}&0\\0&0&0&0&-\frac{1}{RePr}\bar{\mu}\end{pmatrix},$$

$$\mathbf{V}_{xy}=\begin{pmatrix}0&0&0&0&0\\0&0&-\frac{1}{3}\frac{1}{Re}\bar{\mu}&0&0\\0&-\frac{1}{3}\frac{1}{Re}\bar{\mu}&0&0&0\\0&0&0&0&0\\0&0&0&0&0\end{pmatrix},\quad \mathbf{V}_{zz}=\begin{pmatrix}0&0&0&0&0\\0&-\frac{1}{Re}\bar{\mu}&0&0&0\\0&0&-\frac{1}{Re}\bar{\mu}&0&0\\0&0&0&-\frac{4}{3}\frac{1}{Re}\bar{\mu}&0\\0&0&0&0&-\frac{1}{RePr}\bar{\mu}\end{pmatrix},$$

$$\mathbf{V}_{xz}=\begin{pmatrix}0&0&0&0&0\\0&0&0&-\frac{1}{3}\frac{1}{Re}\bar{\mu}&0\\0&0&0&0&0\\0&-\frac{1}{3}\frac{1}{Re}\bar{\mu}&0&0&0\\0&0&0&0&0\end{pmatrix},\quad \mathbf{V}_{yz}=\begin{pmatrix}0&0&0&0&0\\0&0&0&0&0\\0&0&0&-\frac{1}{3}\frac{1}{Re}\bar{\mu}&0\\0&0&-\frac{1}{3}\frac{1}{Re}\bar{\mu}&0&0\\0&0&0&0&0\end{pmatrix},$$

$$\mathbf{\Gamma}_{xyz}=\begin{pmatrix}1&0&0&0&0\\0&\bar{\rho}&0&0&0\\0&0&\bar{\rho}&0&0\\0&0&0&\bar{\rho}&0\\\frac{1-\gamma}{\gamma}\bar{T}&0&0&0&\frac{\bar{\rho}}{\gamma}\end{pmatrix},\quad \mathbf{A}_{xyz}=\begin{pmatrix}a_{11}&a_{12}&0&0&0\\a_{21}&a_{22}&a_{23}&a_{24}&a_{25}\\0&a_{32}&a_{33}&0&a_{35}\\0&a_{42}&0&a_{44}&a_{45}\\a_{51}&a_{52}&a_{53}&a_{54}&a_{55}\end{pmatrix},$$

where

$$a_{11}=\bar{u},\qquad a_{12}=\bar{\rho},\qquad a_{21}=\frac{1}{\gamma Ma^2}\bar{T},$$

$$
\begin{aligned}
&a_{22}=\bar{\rho}\bar{u}, && a_{23}=-\frac{1}{Re}\frac{\partial\bar{\mu}}{\partial y}, && a_{24}=-\frac{1}{Re}\frac{\partial\bar{\mu}}{\partial y},\\
&a_{25}=\frac{1}{\gamma Ma^2}\bar{\rho}+\frac{1}{Re}\tau\Big(\frac{2}{3}\frac{\partial\bar{v}}{\partial y}+\frac{2}{3}\frac{\partial\bar{w}}{\partial z}\Big), && a_{32}=\frac{2}{3}\frac{1}{Re}\frac{\partial\bar{\mu}}{\partial y}, && a_{33}=\bar{\rho}\bar{u},\\
&a_{35}=-\frac{1}{Re}\tau\frac{\partial\bar{\mu}}{\partial y}, && a_{42}=\frac{2}{3}\frac{1}{Re}\frac{\partial\bar{\mu}}{\partial z}, && a_{44}=\bar{\rho}\bar{u},\\
&a_{45}=-\frac{1}{Re}\tau\frac{\partial\bar{\mu}}{\partial z}, && a_{51}=\frac{1-\gamma}{\gamma}\bar{u}\bar{T},\\
&a_{52}=\frac{(\gamma-1)Ma^2}{Re}\left(\frac{4}{3}\bar{\mu}\frac{\partial\bar{v}}{\partial y}+\frac{4}{3}\bar{\mu}\frac{\partial\bar{w}}{\partial z}\right), && a_{53}=-\frac{(\gamma-1)Ma^2}{Re}\left(2\bar{\mu}\frac{\partial\bar{\mu}}{\partial y}\right),\\
&a_{54}=-\frac{(\gamma-1)Ma^2}{Re}\left(2\bar{\mu}\frac{\partial\bar{\mu}}{\partial z}\right), && a_{55}=\frac{1}{\gamma}\bar{\rho}\bar{u}.
\end{aligned}
$$

For

$$
\mathbf{B}_{xyz}=\begin{pmatrix}
b_{11} & 0 & b_{13} & 0 & 0\\
0 & b_{22} & 0 & 0 & b_{25}\\
b_{31} & 0 & b_{33} & b_{34} & b_{34}\\
0 & 0 & b_{43} & b_{44} & b_{45}\\
b_{51} & b_{52} & b_{53} & b_{54} & b_{55}
\end{pmatrix},
$$

where

$$
\begin{aligned}
&b_{11}=\bar{v}, && b_{13}=\bar{\rho},\\
&b_{22}=\bar{\rho}\bar{v}-\frac{1}{Re}\frac{\partial\bar{\mu}}{\partial y}, && b_{25}=-\frac{1}{Re}\tau\frac{\partial\bar{u}}{\partial y},\\
&b_{31}=\frac{1}{\gamma Ma^2}\bar{T}, && b_{33}=\bar{\rho}\bar{v}-\frac{4}{3}\frac{1}{Re}\frac{\partial\bar{\mu}}{\partial y},\\
&b_{34}=-\frac{1}{Re}\frac{\partial\bar{\mu}}{\partial z}, && b_{35}=\frac{1}{\gamma Ma^2}\bar{\rho}-\frac{1}{Re}\tau\Big(\frac{4}{3}\frac{\partial\bar{v}}{\partial y}-\frac{2}{3}\frac{\partial\bar{w}}{\partial z}\Big),\\
&b_{43}=\frac{2}{3}\frac{1}{Re}\frac{\partial\bar{\mu}}{\partial z}, && b_{44}=\bar{\rho}\bar{v}-\frac{1}{Re}\frac{\partial\bar{\mu}}{\partial y},\\
&b_{45}=-\frac{1}{Re}\tau\left(\frac{\partial\bar{w}}{\partial y}+\frac{\partial\bar{v}}{\partial z}\right), && b_{51}=\frac{1-\gamma}{\gamma}\bar{v}\bar{T},\\
&b_{52}=-\frac{(\gamma-1)Ma^2}{Re}\left(2\bar{\mu}\frac{\partial\bar{u}}{\partial y}\right), && b_{53}=-\frac{(\gamma-1)Ma^2}{Re}\left(\frac{8}{3}\bar{\mu}\frac{\partial\bar{v}}{\partial y}-\frac{4}{3}\bar{\mu}\frac{\partial\bar{w}}{\partial z}\right),\\
&b_{54}=-\frac{(\gamma-1)Ma^2}{Re}\left[2\bar{\mu}\left(\frac{\partial\bar{w}}{\partial y}+\frac{\partial\bar{v}}{\partial z}\right)\right], && b_{55}=\frac{1}{\gamma}\bar{\rho}\bar{v}-\frac{1}{RePr}\left(\frac{\partial\bar{\mu}}{\partial y}+\tau\frac{\partial\bar{T}}{\partial y}\right).
\end{aligned}
$$

For

$$\mathbf{C}_{xyz}=\begin{pmatrix} c_{11} & 0 & 0 & c_{14} & 0 \\ 0 & c_{22} & 0 & 0 & c_{25} \\ 0 & 0 & c_{33} & c_{34} & c_{35} \\ c_{41} & 0 & c_{43} & c_{44} & c_{45} \\ c_{51} & c_{52} & c_{53} & c_{54} & c_{55} \end{pmatrix},$$

where

$$c_{11}=\bar{w}, \quad c_{14}=\bar{\rho}, \quad c_{22}=\bar{\rho}\bar{w}-\frac{1}{Re}\frac{\partial\bar{\mu}}{\partial z},$$
$$c_{25}=-\frac{1}{Re}\tau\frac{\partial\bar{u}}{\partial z}, \quad c_{33}=\bar{\rho}\bar{w}-\frac{1}{Re}\frac{\partial\bar{\mu}}{\partial z}, \quad c_{34}=\frac{2}{3}\frac{1}{Re}\frac{\partial\bar{\mu}}{\partial y},$$
$$c_{35}=-\frac{1}{Re}\tau\left(\frac{\partial\bar{w}}{\partial y}+\frac{\partial\bar{v}}{\partial z}\right), \quad c_{41}=\frac{1}{\gamma Ma^2}\bar{T}, \quad c_{43}=-\frac{1}{Re}\frac{\partial\bar{\mu}}{\partial y},$$
$$c_{44}=\bar{\rho}\bar{w}-\frac{4}{3}\frac{1}{Re}\frac{\partial\bar{\mu}}{\partial z}, \quad c_{45}=\frac{1}{\gamma Ma^2}\bar{\rho}-\frac{1}{Re}\tau\Big(-\frac{2}{3}\frac{\partial\bar{v}}{\partial y}+\frac{4}{3}\frac{\partial\bar{w}}{\partial z}\Big), \quad c_{51}=\frac{1-\gamma}{\gamma}\bar{w}\bar{T},$$
$$c_{52}=-\frac{(\gamma-1)Ma^2}{Re}\left(2\bar{\mu}\frac{\partial\bar{u}}{\partial z}\right), \quad c_{53}=-\frac{(\gamma-1)Ma^2}{Re}\left[2\bar{\mu}\left(\frac{\partial\bar{w}}{\partial y}+\frac{\partial\bar{v}}{\partial z}\right)\right],$$
$$c_{54}=-\frac{(\gamma-1)Ma^2}{Re}\left(\frac{8}{3}\bar{\mu}\frac{\partial\bar{w}}{\partial z}-\frac{4}{3}\bar{\mu}\frac{\partial\bar{v}}{\partial y}\right), \quad c_{55}=\frac{1}{\gamma}\bar{\rho}\bar{w}-\frac{1}{RePr}\left(\frac{\partial\bar{\mu}}{\partial z}+\tau\frac{\partial\bar{T}}{\partial z}\right).$$

For

$$\mathbf{D}_{xyz}=\begin{pmatrix} d_{11} & 0 & d_{13} & d_{14} & 0 \\ d_{21} & 0 & d_{23} & d_{24} & d_{25} \\ d_{31} & 0 & d_{33} & d_{34} & d_{35} \\ d_{41} & 0 & d_{43} & d_{44} & d_{45} \\ d_{51} & 0 & d_{53} & d_{54} & d_{55} \end{pmatrix},$$

where

$$d_{11}=\frac{\partial\bar{v}}{\partial y}+\frac{\partial\bar{w}}{\partial z}, \quad d_{13}=\frac{\partial\bar{\rho}}{\partial y}, \quad d_{14}=\frac{\partial\bar{\rho}}{\partial z}, \quad d_{21}=\bar{v}\frac{\partial\bar{u}}{\partial y}+\bar{w}\frac{\partial\bar{u}}{\partial z}, \quad d_{23}=\bar{\rho}\frac{\partial\bar{u}}{\partial y},$$
$$d_{24}=\bar{\rho}\frac{\partial\bar{u}}{\partial z}, \quad d_{25}=-\frac{1}{Re}\frac{\partial\tau}{\partial y}\frac{\partial\bar{u}}{\partial y}-\frac{1}{Re}\frac{\partial\tau}{\partial z}\frac{\partial\bar{u}}{\partial z}-\frac{1}{Re}\tau\left(\frac{\partial^2\bar{u}}{\partial y^2}+\frac{\partial^2\bar{u}}{\partial z^2}\right),$$
$$d_{31}=\bar{v}\frac{\partial\bar{v}}{\partial y}+\bar{w}\frac{\partial\bar{v}}{\partial z}+\frac{1}{\gamma Ma^2}\frac{\partial\bar{T}}{\partial y}, \quad d_{33}=\bar{\rho}\frac{\partial\bar{v}}{\partial y}, \quad d_{34}=\bar{\rho}\frac{\partial\bar{v}}{\partial z},$$
$$d_{35}=\frac{1}{\gamma Ma^2}\frac{\partial\bar{\rho}}{\partial y}-\frac{1}{Re}\frac{\partial\tau}{\partial y}\left(\frac{4}{3}\frac{\partial\bar{v}}{\partial y}-\frac{2}{3}\frac{\partial\bar{w}}{\partial z}\right)-\frac{1}{Re}\frac{\partial\tau}{\partial z}\left(\frac{\partial\bar{v}}{\partial z}+\frac{\partial\bar{w}}{\partial y}\right)-\frac{1}{Re}\tau\left(\frac{4}{3}\frac{\partial^2\bar{v}}{\partial y^2}+\frac{\partial^2\bar{v}}{\partial z^2}+\frac{1}{3}\frac{\partial^2\bar{w}}{\partial y\partial z}\right),$$
$$d_{41}=\bar{v}\frac{\partial\bar{w}}{\partial y}+\bar{w}\frac{\partial\bar{w}}{\partial z}+\frac{1}{\gamma Ma^2}\frac{\partial\bar{T}}{\partial z}, \quad d_{43}=\bar{\rho}\frac{\partial\bar{w}}{\partial y}, \quad d_{44}=\bar{\rho}\frac{\partial\bar{w}}{\partial z},$$

$$
\begin{aligned}
d_{45}&=\frac{1}{\gamma Ma^2}\frac{\partial\bar{\rho}}{\partial z}-\frac{1}{Re}\frac{\partial\tau}{\partial y}\left(\frac{\partial\bar{v}}{\partial z}+\frac{\partial\bar{w}}{\partial y}\right)-\frac{1}{Re}\frac{\partial\tau}{\partial z}\left(-\frac{2}{3}\frac{\partial\bar{v}}{\partial y}+\frac{4}{3}\frac{\partial\bar{w}}{\partial z}\right)-\frac{1}{Re}\tau\left(\frac{\partial^2\bar{w}}{\partial y^2}+\frac{4}{3}\frac{\partial^2\bar{w}}{\partial z^2}+\frac{1}{3}\frac{\partial^2\bar{v}}{\partial y\partial z}\right),\\
d_{51}&=\frac{1}{\gamma}\left(\bar{v}\frac{\partial\bar{T}}{\partial y}+\bar{w}\frac{\partial\bar{T}}{\partial z}\right),\quad d_{53}=\frac{1}{\gamma}\bar{\rho}\frac{\partial\bar{T}}{\partial y}+\frac{1-\gamma}{\gamma}\bar{T}\frac{\partial\bar{\rho}}{\partial y},\quad d_{54}=\frac{1}{\gamma}\bar{\rho}\frac{\partial\bar{T}}{\partial z}+\frac{1-\gamma}{\gamma}\bar{T}\frac{\partial\bar{\rho}}{\partial z},\\
d_{55}&=\frac{1-\gamma}{\gamma}\left(\bar{v}\frac{\partial\bar{\rho}}{\partial y}+\bar{w}\frac{\partial\bar{\rho}}{\partial z}\right)-\frac{1}{RePr}\left(\frac{\partial\tau}{\partial y}\frac{\partial\bar{T}}{\partial y}+\frac{\partial\tau}{\partial z}\frac{\partial\bar{T}}{\partial z}+\tau\frac{\partial^2\bar{T}}{\partial y^2}+\tau\frac{\partial^2\bar{T}}{\partial z^2}\right)\\
&\quad-\frac{(\gamma-1)Ma^2}{Re}\left[\frac{4}{3}\tau\left(\frac{\partial\bar{v}}{\partial y}\right)^2+\frac{4}{3}\tau\left(\frac{\partial\bar{w}}{\partial z}\right)^2-\frac{4}{3}\tau\frac{\partial\bar{v}}{\partial y}\frac{\partial\bar{w}}{\partial z}\right.\\
&\quad\left.+\tau\left(\frac{\partial\bar{u}}{\partial y}\right)^2+\tau\left(\frac{\partial\bar{u}}{\partial z}\right)^2+\tau\left(\frac{\partial\bar{v}}{\partial z}\right)^2+\tau\left(\frac{\partial\bar{w}}{\partial y}\right)^2+2\tau\frac{\partial\bar{v}}{\partial z}\frac{\partial\bar{w}}{\partial y}\right].
\end{aligned}
$$

The variable τ represents the linear coefficient of perturbation viscosity to perturbation temperature, i.e., $\mu'=\tau T'$, and it depends on the basic flow temperature $\bar{T}$.

Appendix B: The coefficient matrices in Eq. (2.6)

The coefficient matrices in Eq. (2.6) are provided as below

$$
\begin{aligned}
\mathbf{A}_{\xi\eta\zeta}&=\mathbf{A}+J\left[\frac{\partial}{\partial\eta}\left(\frac{\eta_Y}{J}\right)+\frac{\partial}{\partial\zeta}\left(\frac{\zeta_Y}{J}\right)\right]\mathbf{V}_{XY}+J\left[\frac{\partial}{\partial\eta}\left(\frac{\eta_Z}{J}\right)+\frac{\partial}{\partial\zeta}\left(\frac{\zeta_Z}{J}\right)\right]\mathbf{V}_{XZ},\\
\mathbf{B}_{\xi\eta\zeta}&=\eta_Y\mathbf{B}+\eta_Z\mathbf{C}+J\left[\frac{\partial}{\partial\eta}\left(\frac{\eta_Y^2}{J}\right)+\frac{\partial}{\partial\zeta}\left(\frac{\eta_Y\zeta_Y}{J}\right)\right]\mathbf{V}_{yy}+J\left[\frac{\partial}{\partial\eta}\left(\frac{\eta_Z^2}{J}\right)+\frac{\partial}{\partial\zeta}\left(\frac{\eta_Z\zeta_Z}{J}\right)\right]\mathbf{V}_{ZZ}\\
&\quad+J\left[\frac{\partial}{\partial\eta}\left(\frac{\eta_Y\eta_Z}{J}\right)+\frac{\partial}{\partial\zeta}\left(\frac{\eta_Y\zeta_Z}{J}\right)\right]\mathbf{V}_{YZ},\\
\mathbf{C}_{\xi\eta\zeta}&=\zeta_Y\mathbf{B}+\zeta_Z\mathbf{C}+J\left[\frac{\partial}{\partial\eta}\left(\frac{\eta_Y\zeta_Y}{J}\right)+\frac{\partial}{\partial\zeta}\left(\frac{\zeta_Y^2}{J}\right)\right]\mathbf{V}_{YY}+J\left[\frac{\partial}{\partial\eta}\left(\frac{\eta_Z\zeta_Z}{J}\right)+\frac{\partial}{\partial\zeta}\left(\frac{\zeta_Z^2}{J}\right)\right]\mathbf{V}_{ZZ}\\
&\quad+J\left[\frac{\partial}{\partial\eta}\left(\frac{\zeta_Y\eta_Z}{J}\right)+\frac{\partial}{\partial\zeta}\left(\frac{\zeta_Y\zeta_Z}{J}\right)\right]\mathbf{V}_{YZ},\\
\mathbf{V}_{\xi\xi}&=\mathbf{V}_{XX},\quad\mathbf{V}_{\eta\eta}=\eta_Y^2\mathbf{V}_{YY}+\eta_z^2\mathbf{V}_{zz}+\eta_Y\eta_Z\mathbf{V}_{YZ},\quad\mathbf{V}_{\zeta\zeta}=\zeta_Y^2\mathbf{V}_{YY}+\zeta_Z^2\mathbf{V}_{ZZ}+\zeta_Y\zeta_Z\mathbf{V}_{YZ},\\
\mathbf{V}_{\xi\eta}&=\eta_Y\mathbf{V}_{XY}+\eta_Z\mathbf{V}_{XZ},\quad\mathbf{V}_{\xi\zeta}=\zeta_Y\mathbf{V}_{XY}+\zeta_Z\mathbf{V}_{XZ},\\
\mathbf{V}_{\eta\zeta}&=2\eta_Y\zeta_Y\mathbf{V}_{YY}+2\eta_Z\zeta_Z\mathbf{V}_{ZZ}+(\eta_Y\zeta_Z+\eta_Z\zeta_Y)\mathbf{V}_{YZ}.
\end{aligned}
$$

The variable J is the Jacobian determinant, which can be expressed as

$$
J=1\Big/\begin{vmatrix}Y_\eta & Y_\zeta\\ Z_\eta & Z_\zeta\end{vmatrix}=1/\left[Y_\eta Z_\zeta-Y_\zeta Z_\eta\right].
$$

Acknowledgements

This work was supported by the National Key Research and Development Program of China (Grant No. 2016YFA0401200) and by the National Natural Science Foundation of China (Grant Nos. 91952301, 11672204, 12072230, and 11732011).

References

[1] F. LI, M. CHOUDHARI, C. L. CHANG, J. WHITE, R. KIMMEL, D. ADAMCZAK, M. BORG, S. STANFIELD, AND M. SMITH, *Stability analysis for hifire experiments,* 42nd AIAA Fluid Dynamics Conference and Exhibit, (2012).

[2] J. WANG, P. ZIADÉ, G. HUANG, AND P. E. SULLIVAN, *Bi-global stability analysis in curvilinear coordinates,* Phys. Fluids, 31 (2019), 105105.

[3] X. LI, J. CHEN, Z. HUANG, Q. YANG, AND G. XU, *Stability analysis and transition prediction of streamwise vortices over a yawed cone at Mach 6,* Phys. Fluids, 32 (2020), 124110.

[4] R. SONG, L. ZHAO, AND Z. HUANG, *Improvement of the parabolized stability equation to predict the linear evolution of disturbances in three-dimensional boundary layers based on ray tracing theory,* Phys. Rev. Fluids, 5 (2020), 033901.

[5] I. LYTTLE, AND H. REED, *Use of transition correlations for three-dimensional boundary layers within hypersonic flows,* Fluid Dynamics Conference, (1995).

[6] R. L. KIMMEL, M. A. KLEIN, AND S. N. SCHWOERKE, *Three-dimensional hypersonic laminar boundary-layer computations for transition experiment design,* J. Spacecr. Rockets, 34 (1997), pp. 409-–415.

[7] J. POGGIE, R. L. KIMMEL, AND S. N. STEPHEN, *Traveling instability waves in a Mach 8 flow over an elliptic cone,* AIAA J., 38 (2000), pp. 251—258.

[8] J. SCHMISSEUR, S. SCHNEIDER, AND S. COLLICOTT, *Supersonic boundary-layer response to optically generated freestream disturbances,* Exp. Fluids, 33 (2002), pp. 225—232.

[9] M. HUNTLEY, AND A. SMITS, *Transition studies on an elliptic cone in Mach 8 flow using filtered Rayleigh scattering,* Euro. J. Mech. B Fluids, 19 (2000), pp. 695-–706.

[10] R. GOSSE, AND R. KIMMEL, *CFD study of three-dimensional hypersonic laminar boundary layer transition on a Mach 8 elliptic cone,* 39th AIAA Fluid Dynamics Conference, (2009), 4053.

[11] P. PAREDES, R. GOSSE, V. THEOFILIS, AND R. KIMMEL, *Linear modal instabilities of hypersonic flow over an elliptic cone,* J. Fluid Mech., 804 (2016), pp. 442—466.

[12] D. J. DINZL, AND G. V. CANDLER, *Direct simulation of hypersonic crossflow instability on an elliptic cone,* AIAA J., 55 (2017), pp. 1-–14.

[13] M. CHOUDHARI, F. LI, AND P. PAREDES, *Streak Instabilities on HIFiRE-5 Elliptic Cone,* AIAA SciTech. 2020 Forum, (2020).

[14] T. J. JULIANO, J. S. JEWELL, AND R. L. KIMMEL, *Hifire-5b boundary-layer transition length and turbulent overshoot,* J. Spacecr. Rockets, 9 (2021), pp. 1-–19.

[15] L. QIAO, J. XU, J. BAI, AND Y. ZHANG, *Fully local transition closure model for hypersonic boundary layers considering crossflow effects,* AIAA J., 59 (2021), pp. 1692-–1706.

[16] R. GOSSE, AND R. KIMMEL, *CFD Study of the HIFiRE-5 Flight Experiment,* 40th Fluid Dynamics Conference and Exhibit, (2010), 4854.

[17] B. WHEATON, T. JULIANO, D. BERRIDGE, A. CHOU, P. GILBERT, P. CASPER, L. STEEN, S. SCHNEIDER, AND H. JOHNSON, *Instability and transition measurements in the Mach-6 quiet tunnel,* AIAA Fluid Dynamics Conference, (2009), 3559.

[18] T. JULIANO, M. BORG, AND S. SCHNEIDER, *Quiet Tunnel Measurements of HIFiRE-5 Boundary-Layer Transition,* AIAA J., 53 (2015), pp. 832-–846.
[19] W. ZHANG, AND R. SAMTANEY, *Biglobal linear stability analysis on low-Re flow past an airfoil at high angle of attack,* Phys. Fluids, 28 (2016), pp. 290—305.
[20] A. MOYES, P. PAREDES, T. KOCIAN, AND H. REED, *Secondary instability analysis of crossflow on a hypersonic yawed straight circular cone,* J. Fluid Mech., 812 (2017), pp. 370-–397.
[21] D. XIAO, H. BORRADAILE, K. CHOI, L. FENG, J. WANG, AND X. MAO, *Bypass transition in a boundary layer flow induced by plasma actuators,* J. Fluid Mech., 929 (2021), A6.
[22] M. CHOUDHARI, C. L. CHANG, T. L. F. JENTINK, K. BERGER, G. CANDLER, AND R. KIMMEL, *Transition analysis for the HIFiRE-5 vehicle,* 39th AIAA Fluid Dynamics Conference, (2009), 4056.
[23] P. PAREDES, AND V. THEOFILIS, *Spatial linear global instability analysis of the HIFiRE-5 elliptic cone model flow,* 43rd AIAA Fluid Dynamics Conference, (2013), 2880.
[24] P. PAREDES, AND V. THEOFILIS, *Traveling global instabilities on the HIFiRE-5 elliptic cone model flow,* Aerospace Sciences Meeting, (2014).
[25] P. PAREDES, AND V. THEOFILIS, *Centerline instabilities on the hypersonic international flight research experimentation HIFiRE-5 elliptic cone model,* J. Fluid Struct., 53 (2015), pp. 36-–49.
[26] S. ZHANG, The Instability and Wave Propagation in the Hypersonic 2 : 1 Elliptic Cone Boundary Layer, (Ph.D. Thesis) (Tianjin: Tianjin University) (in Chinese), (2016).
[27] X. LI, S. ZHANG, J. LIU, Z. HUANG, J. LUO, AND Y. ZHANG, *Two dimensional global stability analysis of hypersonic elliptical cone short axis streamwise vortices,* Acta Aerodynamica Sinica, 036 (2018), pp. 265-–272.
[28] A. MOYES, AND H. L. REED, *Nonlinear boundary-layer stability analysis of BOLT and HIFiRE-5,* AIAA Aviation 2019 Forum, (2019).
[29] L. ZHAO, Y. YANG, AND R. SONG, *Non-modal instability and transition of hypersonic boundary layer over a blunt flat-plate,* The Chinese Congress of Theoretical and Applied Mechanics (in Chinese) (2019).
[30] J. CHEN, S. DONG, X. CHEN, X. YUAN, AND G. XU, *Stationary cross-flow breakdown in a high-speed swept-wing boundary layer,* Phys. Fluids, 33 (2021), 024108.
[31] X. LI, Q. YANG, J. CHEN, Z. HUANG, G. XU, AND G. TU, *Effect of three-dimensional smooth humps on hypersonic boundary layer instability of streamwise vortices over a yawed cone,* Phys. Fluids, 33 (2021), 064109.
[32] Y. ZHANG, AND J. LUO, *Application of Arnoldi method to boundary layer instability,* Chin. Phys. B, 24 (2015), 124701.
[33] R. B. LEHOUCQ, D. C. SORENSEN, AND C. YANG, *ARPACK users guide: solution of large scale eigenvalue problems by implicitly restarted Arnoldi methods,* J. Chem. Phys., 157 (1998), 044119.
[34] L. ZHAO, Study on Instability of Stationary Crossflow Vortices in Hypersonic Swept Blunt Plate Boundary Layer, (Ph.D. Thesis) (Tianjin: Tianjin University) (in Chinese), (2017).
[35] R. SONG, L. ZHAO, AND Z. HUANG, *Secondary instability of stationary Görtler vortices originating from first/second Mack mode,* Phys. Fluids, 32, (2020), 034109.
[36] Y. ZHANG, X. CHEN, AND J. LUO, *Study of secondary instability of a streaky boundary layer under spanwise-localized free-stream vortical disturbances,* Adv. Appl. Math. Mech., 11 (2019), pp. 686-–699.
[37] M. GASTER, *A note on the relation between temporally increasing and spatially increasing disturbances in hydrodynamic stability,* J. Fluid Mech., 14, (1962), pp. 222—224.
[38] A. M. O. SMITH, AND N. GAMBERONI, *Transition, pressure gradient, and stability theory,* Douglas Aircraft Co., Report ES 26388 (1956).

[39] J. VAN INGEN, *A suggested semi-empirical method for the calculation of boundary layer transition region*, Department of Aeronautical Engineering, University of Technology, Delft, Report No. VTH-74, (1956).